# Computer-Aided Diagnosis in Phase Contrast Imaging X-Ray Computed Tomography for Quantitative Characterization of *ex vivo* Human Patellar Cartilage

**Mahesh B. Nagarajan**[*],
Department of Imaging Sciences and Biomedical Engineering, University of Rochester, Rochester, NY 14627 USA

**Paola Coan**,
Faculty of Medicine and Institute of Clinical Radiology, Ludwig Maximilians University, Munich 80336, Germany, with the Faculty of Physics, Ludwig Maximilians University, Munich 85748, Germany; European Synchrotron Radiation Facility, 38000 Grenoble, France (Paola.Coan@med.uni-muenchen.de)

**Markus B. Huber**,
Department of Imaging Sciences and Biomedical Engineering, University of Rochester, Rochester, NY 14627 USA (mbh@bme.rochester.edu)

**Paul C. Diemoz**,
Faculty of Physics, Ludwig Maximilians University, Munich 85748, Germany and also with the European Synchrotron Radiation Facility, 38000 Grenoble, France (p.diemoz@ucl.ac.uk)

**Christian Glaser**, and
Faculy of Medicine and Institute of Clinical Radiology, Ludwig Maximilians University, Munich 80336, Germany (Christian.glaser@med.uni-muenchen.de)

**Axel Wismüller**
Department of Imaging Science and Biomedical Engineering, University of Rochester, Rochester, NY 14627 USA; Department of Radiology, Ludwig Maximilians University, Munich 80336, Germany (axel_wismueller@urmc.rochester.edu)

## Abstract

Visualization of *ex vivo* human patellar cartilage matrix through the phase contrast imaging X-ray computed tomography (PCI-CT) has been previously demonstrated. Such studies revealed osteoarthritis-induced changes to chondrocyte organization in the radial zone. This study investigates the application of texture analysis to characterizing such chondrocyte patterns in the presence and absence of osteoarthritic damage. Texture features derived from Minkowski

functionals (MF) and gray-level co-occurrence matrices (GLCM) were extracted from 842 regions of interest (ROI) annotated on PCI-CT images of *ex vivo* human patellar cartilage specimens. These texture features were subsequently used in a machine learning task with support vector regression to classify ROIs as healthy or osteoarthritic; classification performance was evaluated using the area under the receiver operating characteristic curve (AUC). The best classification performance was observed with the MF features perimeter (AUC: $0.94 \pm 0.08$) and "Euler characteristic" (AUC: $0.94 \pm 0.07$), and GLCM-derived feature "Correlation" (AUC: $0.93 \pm 0.07$). These results suggest that such texture features can provide a detailed characterization of the chondrocyte organization in the cartilage matrix, enabling classification of cartilage as healthy or osteoarthritic with high accuracy.

### Keywords

Gray-level co-occurrence matrix (GLCM); Minkowski functionals (MF); osteoarthritis (OA); phase contrast imaging X-ray computed tomography (PCI-CT); support vector regression (SVR); texture analysis

## I. Introduction

Osteoarthritis (OA) is widely recognized as one of the leading causes of disability worldwide [1]-[3]. This disease is characterized by loss of the articular cartilage, thickening of the underlying subchondral bone, and osteophyte formation. Currently, monitoring OA progression to evaluate patient health and assess the impact of drug intervention is of significant interest. Diagnostic markers that are used for this purpose, such as joint pain or observation of joint space narrowing on conventional radiography, are only sensitive at advanced stages of the disease. It would be desirable to have an imaging modality that could provide early detection and visualization of any degenerative modifications to the cartilage [4]-[8]. Several imaging techniques have been proposed to detect changes in cartilage quality through evaluation of glycosaminoglycan (GAG) content, such as delayed gadolinium-enhanced MR imaging of cartilage (dGEMRIC) [9], $^{23}$Na MRI [10], T1$\rho$ [11], GAG chemical exchange saturation transfer [12], etc. However, none of these techniques currently possess the capability to visualize cartilage matrix structure at a cellular level. In this context, Coan *et al.* demonstrated the ability of phase contrast imaging X-ray computed tomography (PCI-CT) to visualize the internal architecture of the cartilage matrix at micrometer scale resolution in *ex vivo* samples of the human patellae and recorded differences in chondrocyte organization in healthy and osteoarthritic subjects [13].

Phase contrast imaging (PCI) has emerged as a novel X-ray-based imaging approach owing to its ability to provide enhanced image contrast for visualizing structural details in the soft tissue. PCI exploits the fact that X-rays are not just absorbed when passing through matter but also refracted [14], [15]. The phase contrast effect associated with such refraction can be more pronounced than the conventional absorption contrast, specifically for the energy range of X-rays used in diagnostic modalities, and for the soft tissue encountered in clinical studies [16]. This allows PCI to be effective in imaging tissue types where the conventional absorption contrast is either unable to resolve differences between different soft tissue types,

i.e., breast [17], [18], or poor/absent, i.e., cartilage [13], [19], [20]. Among different PCI techniques, we specifically focus on the analyzer-based imaging (ABI) scheme [15], [21], [22] that has been applied in different *ex vivo* breast [17], [18], brain [23], and cartilage studies [13], [19].

We specifically focus on cartilage in the retropatellar joint which has significant potential for enabling early detection of treatable osteoarthritic changes to the cartilage matrix. Patellar cartilage, unlike femoro-tibial cartilage, is the thickest cartilage tissue compartment in the human body which still shows macroscopic differences in appearance between healthy and osteoarthritic states. PCI-CT imaging of *ex vivo* healthy and osteoarthritic specimens of human patellar cartilage matrix revealed specific differences in their internal architecture. Of specific interest was osteoarthritic-induced changes to the chondrocyte organization in the radial zone of the cartilage matrix. Chondrocytes in normal samples maintained a zone specific architecture; this was specifically visualized in the radial zone where the chondrocytes were aligned in a direction perpendicular to the tide mark (also known as Benninghoff's arch). This zone-specific organization of chondrocytes was not observed in osteoarthritic samples and was instead replaced by a more generalized clustering of cells throughout the matrix [13]. The primary goal of this study was to identify quantitative measures that could characterize such differences in chondrocyte patterns and evaluate their ability to serve as diagnostic biomarkers for osteoarthritic-induced changes to the cartilage matrix. In particular, we focus on the use of texture analysis, which to our knowledge, has not been previously used for quantitative analysis of cartilage matrix structure as visualized by PCI-CT.

Texture analysis involves quantifying spatial properties of pixel distributions, i.e., image patterns, from a specified region of interest (ROI). In this study, we pursued two approaches: 1) second-order statistical texture features derived from gray-level co-occurrence matrices (GLCM) [24]; and 2) topological texture features derived from the Minkowski functionals (MF) [25]. GLCM has been previously investigated in a wide range of medical image analysis tasks such as distinguishing pathological patterns from healthy lung tissue on chest CT [26], classifying benign and malignant lesions through characterization of the lesion enhancement pattern on dynamic breast MRI [27], and quantitative analysis of carotid atherosclerotic plaques on ultrasound B-mode scans [28]. However, texture features derived through more novel techniques such as MF can provide a detailed topological characterization of the gray-level pattern being analyzed. This approach has been previously investigated in fibrotic tissue classification on lung CT [29], [30], dynamic characterization of tissue lesions on breast MRI [31], and hip-fracture prediction in post-menopausal women [32].

Given the wide applicability of texture features derived from GLCM and MF to medical image processing tasks, we investigate the ability of such features in quantifying chondrocyte patterns in the radial zone of the cartilage matrix as visualized by PCI-CT. These features are evaluated in their ability to classify ROIs as being normal or osteoarthritic in a machine learning task using support vector regression (SVR) [33], as discussed in the following sections.

## II. Materials and Methods

### A. Samples

The selection of the patellae was based on age of the donor, macroscopic visual inspection, and probing of the cartilage surface at autopsy. Donors older than 40 years were *a priori* excluded for harvest of normal samples; no constraint in age was imposed on potential donors for osteoarthritic samples. A smooth, white, and shiny surface present across the entire patellar cartilaginous surface and prompt resilience to manually performed focal indentation probing were criteria that defined macroscopically normal cartilage. Lack of these criteria in addition to visually perceived defects in the joint surface were used to select osteoarthritic samples. IRB was waived by the institutional review board of the Ludwig Maximilians University, Munich, Germany. Based on these inclusion criteria, two healthy and three osteoarthritic cylinder-shaped osteochondral samples (diameter: 7 mm) were extracted within 48 h postmortem from the lateral facet of the four human patellae using a shell auger. Cylinders were trimmed to a total height of 12 mm including the complete cartilage tissue and the subchondral bone. The samples were continuously rinsed by 0.9% saline during extraction, trimming, and removal of soiling from sawing. During image acquisition, samples were dipped into a 10% formalin solution. The grade of the osteoarthritic samples was assessed to be 3-4 based on a histological standard proposed in [34].

### B. PCI Experimental Setup

The ABI setup consisted of a parallel monochromatic X-ray beam, used to irradiate the sample, and of a perfect crystal, the analyzer, placed between the sample, and the detector [35]. The analyzer acts as an angular filter of the radiation transmitted through the object and only the X-rays traveling in a narrow angle window close to the Bragg condition are diffracted onto the detector [22]. Before being detected, the beam is modulated by the angle-dependent reflectivity of the crystal; its rocking curve (RC) has a full width at half maximum typically of the order of a few microradians. All images were acquired at the half maximum position on one slope of the RC (50% position), which was chosen to achieve the best sensitivity. Further details of the ABI technique used in this study can be found in [13].

Experiments were performed at the Biomedical Beamline (ID17) of the European Synchrotron Radiation Facility (ESRF, France). A highly collimated X-ray beam was produced by a 21-pole wiggler after monochromatization by means of a double Si (111) crystal system and an additional single Si (333) crystal [36]. The emerging, refracted, and scattered radiation from the sample was analyzed with a Si (333) analyzer crystal. Quasi-monochromatic X-rays of 26 keV were used. Given the laminar shape of the stationary synchrotron beam, images were obtained by rotating and vertically scanning the sample through the X-ray beam [37]. The imaging detector used was the Fast Readout Low Noise (FReLoN) CCD camera developed at the ESRF [38]. The X-rays were converted to visible light by a 60 $\mu$m thick Gadox fluorescent screen; this scintillation light was then guided onto a $2048 \times 2048$ pixel $14 \times 14$ m$^2$ CCD (Atmel Corp, U.S.) by lens-based system. The effective pixel size at the object plane was $8 \times 8$ $\mu$m$^2$.

## C. Tomographic Image Reconstruction

To acquire the CT images with synchrotron radiation, the sample was rotated about an axis perpendicular to the incident laminar beam; it was vertically displaced at the end of each rotation to image a different region. Both the beam and the detector were kept stationary; the detector acquisition was synchronized with the sample angular scanning. A flat field normalization was performed for each angular projection image to reduce the effects of the spatial and temporal X-ray beam inhomogeneities. Tomographic images were reconstructed using a direct Hamming filter backprojection algorithm [39]. An image volume of dimensions $1120 \times 1124 \times 805$ was acquired for each specimen and subsequently trimmed to eliminate background regions. For data analysis, coronal slices of slice thickness 8 $\mu$m were reconstructed from the original data and subjected to edge-preserving median filtering with a [5 5] sliding window to smoothen noise artifacts.

## D. Annotation

Chondrocyte patterns were annotated with 2-D square ROIs in the radial zone of the cartilage matrix on the acquired PCI-CT images of all five specimens. In each specimen, special care was taken to ensure that the same cluster of chondrocytes was not captured by different ROIs by ensuring that annotated slices were atleast 32 $\mu$m apart. 842 ROIs were annotated in total, of which 439 were osteoarthritic and 403 were healthy. All ROIs extracted from healthy cases were healthy, while those from the OA cases were abnormal, i.e., no healthy ROIs were extracted from the OA samples in this study. The annotations were made using a square of $101 \times 101$ pixels; ROIs of smaller size (11, 21, …, 91) were then extracted without any manual intervention using the same ROI center. The ground truth was extracted using analysis performed by two independent observers as described in [13]. Examples of a healthy and osteoarthritic ROIs annotated on PCI-CT images are shown in Fig. 1.

## E. Texture Analysis

MF were computed by first binarizing each ROI through the application of several thresholds between its minimum and maximum intensity limits [25]. The number of thresholds applied was a free parameter; a suitable choice for this parameter was investigated here. On each binarized image, three MF, i.e., area, perimeter, and Euler characteristic, were computed as follows:

$$MF_{\text{area}} = n_s \quad (1)$$

$$MF_{\text{perimeter}} = -4n_s + 2n_e \quad (2)$$

$$MF_{Euler} = n_s - n_e + n_v \quad (3)$$

where $n_s$ was the total number of white pixels, $n_e$ was the total number of edges, and $n_v$ was the number of vertices. The area feature recorded the area of the white pixel regions in the binary image, the perimeter measure calculated the length of the boundary of white pixel regions, and the Euler characteristic was a measure of connectivity between the white pixel

regions. Further explanation of how these formulae were derived can be found in [25]. Once computed for every binary image derived from a specific ROI, these values were stored in three high-dimensional vectors corresponding to each MF. This is further illustrated in Fig. 2.

GLCM were extracted from the ROIs as described in [24]. The interpixel distance $d$ was a free parameter; a suitable choice for this parameter was investigated here. On each ROI, the gray-levels were quantized to 32 gray-level values. GLCMs were then generated in the four principal directions and then, summed up element-wise resulting in one nondirectional GLCM. From this, the least correlated and most frequently used statistical features were computed, i.e., absolute value, entropy, contrast, energy, correlation, and homogeneity [40].

*Statistical moments* of the gray-level distributions within the ROIs, i.e., mean and standard deviation, were used both individually and combined as a 2-D vector to serve as a baseline for comparison with texture features derived from GLCM and MF.

## F. Classification

The extraction of texture features was followed by a supervised learning step where the ROIs were classified as healthy or osteoarthritic. We note here that since GLCM features are 1-D while MF feature vectors are 20-D, classification was univariate for GLCM features and multivariate for MF. In this paper, SVR with a radial basis function kernel was used for the machine learning task [33]. The SVR implementation was taken from the libSVM library [41].

Owing to the practical limitations imposed by the small size of the patient population used in this study, we specified the following patient constraints to the supervised learning step: 1) ROIs from the same patient were not simultaneously used in both training and test sets; and 2) the same number of ROIs was used from every patient to ensure that the classifier did not get overtrained on patterns from a specific patient. Based on these constraints, each iteration of the supervised learning step involved randomly sub-sampling 100 ROIs from each of the five patients and randomly designating one of the healthy and osteoarthritic subjects as the test set (the other samples comprised the training set). Such a strategy ensured that training sets used in different iterations of supervised learning were not identical despite the patient constraint. In the training phase, models were created from labeled data by employing a random sub-sampling cross-validation strategy where the training set was further split into 70% training samples and 30% validations samples—the purpose of the training was to determine the optimal classifier parameters that best captured the boundaries between the two classes of ROIs. The free parameters for the classifier used in this study were the cost parameter for SVR and the shape parameter of the radial basis function kernel. Then, during the testing phase, the optimized classifier predicted the class of ROIs in the independent test set. A receiver operating characteristic (ROC) curve was generated and used to compute the area under the ROC curve (AUC) which served as a measure of classifier performance on the independent test set.

## G. Statistical Analysis

A Wilcoxon signed-rank test was used to compare two AUC distributions corresponding to different texture features. Significance thresholds were adjusted for multiple comparisons using the Holm-Bonferroni correction to achieve an overall type I error rate (significance level) less than $\alpha$ (where $\alpha = 0.05$) [42], [43].

Texture, classifier, and statistical analysis were implemented using Matlab 2010a (The MathWorks, Natick, MA, USA).

# III. Results

## A. Free Parameter Exploration

Fig. 3 shows the classification performance of the GLCM-derived features when computed with different interpixel distances ($d = 1, 2, 3, 4, 5$). The texture features were computed from ROIs of size $101 \times 101$ pixels. As seen here, the classification performance deteriorated as the interpixel distance was increased. The best classification performance was noted with GLCM feature *correlation* ($0.93 \pm 0.07$) for $d = 1$.

Fig. 4 shows the classification performance of topological texture features derived from MF when extracted using different number of thresholds. As with GLCM, these texture features were also computed from ROIs of size $101 \times 101$ pixels. The best classification performance was observed for features *perimeter* ($0.94 \pm 0.08$) and *Euler characteristic* ($0.94 \, 0.07$) obtained with 20 thresholds; increasing the number of±thresholds further did not improve the performance achieved.

## B. Classification Performance Comparison

Table I compares the classification performance achieved with the statistical moments, GLCM-derived features (using $d = 1$) and MF (with 20 thresholds). The best performance was observed with MF perimeter ($0.94 \pm 0.08$) and Euler characteristic ($0.94 \pm 0.07$), and GLCM feature correlation ($0.93 \pm 0.07$). Both features significantly outperformed all statistical moments ($p < 10^{-4}$). Standard deviation produced the best performance from the statistical moment features ($0.66 \pm 0.06$). All texture features were computed from ROIs of size $101 \times 101$ pixels.

## C. Impact of ROI Size

Fig. 5 shows the effect of ROI size on the classification performance of the best feature from GLCM (correlation), MF (Euler characteristic) and statistical moments (mean and standard deviation). The performance for all features was observed to be best when texture features were extracted from ROIs of the largest size used in this study, i.e., $101 \times 101$ pixels. For ROIs of size $51 \times 51$ pixels and greater, both Euler characteristic and correlation achieve comparable classification performance. However, for smaller sized ROIs, correlation outperformed Euler characteristic. Regardless of ROI size, both features significantly outperformed standard deviation ($p < 10^{-4}$).

## IV. Discussion

PCI has emerged as a novel X-ray-based imaging modality for providing enhanced image contrast in certain biological tissue types [13], [17]-[20]. In the field of cartilage imaging, Coan *et al.* previously demonstrated the ability of PCI-CT to visualize structural details of the cartilage matrix with high-spatial resolution, and reported differences in chondrocyte organization within the cartilage matrix, specifically in the radial zone [13]. In this study, we investigated the use of texture features derived from topological and statistical approaches, i.e., MF and GLCM, in characterizing such differences and potentially serving as diagnostic bio-markers for OA. Our results show that such textural descriptors can classify chondrocyte patterns as being healthy or osteoarthritic with high accuracy.

MF enable the characterization of the underlying topology as a function of the gray-level threshold by capturing information pertaining to size (area), boundary (perimeter), and connectivity (Euler characteristic). In this study, such detailed topological information was stored in high-dimensional feature vectors which were subsequently processed in a machine learning task. The best classification performance was noted with Euler characteristic which suggests that connectivity can serve as a major distinguishing factor between healthy and osteoarthritic ROIs. This is supported by the fact that the chondrocytes are more clustered in the osteoarthritic ROIs than they are in healthy ROIs; such a clustering could influence the topology of the gray-level patterns being captured by the ROIs. The ability of Euler Characteristic to distinguish between healthy and osteoarthritic ROIs is further illustrated in Fig. 6. We also note that the MF area performed the worst suggesting that analyzing the behavior of pixel regions with high intensity values as a function of the gray-level threshold does not really contribute toward distinguishing between the two classes of chondrocyte patterns. This could also suggest that topological characterization of these chondrocyte patterns needs to be sufficiently complex in order to accurately distinguish between the two classes.

Most features derived from GLCM or statistical moments such as mean and standard deviation did not yield a comparable performance to Euler characteristic in terms of classifying healthy and osteoarthritic ROIs, as seen in Table I. The failure of such statistical features adds further credence to the complexity of the pattern classification problem being investigated in this study; simpler feature descriptors that account for the distribution of intensity values, brightness, etc, alone are not sufficient to characterize the differences between the two classes of chondrocyte patterns. We do note one exception, i.e., GLCM feature correlation, that exhibited comparable classification performance to MF Euler characteristic. This feature measures the gray-level linear dependencies between neighboring pixels [24]. Since chondrocytes are more clustered in osteoarthritic ROIs, these ROIs tend to exhibit higher correlation values than healthy ROIs which capture more extra cellular space. This could explain the effectiveness of the correlation feature in distinguishing between healthy and osteoarthritic ROIs annotated on PCI-CT images.

The impact of the ROI size on the classification performance of different features was also investigated in this study. The best performance was achieved with the largest ROI size, i.e., $101 \times 101$ pixels, as shown in Fig. 5. Such ROIs would capture larger portions of the

chondrocyte patterns being investigated leading to better characterization by the texture features. While performance deteriorates as the ROI size is reduced, AUC values of 0.9 are noted at an ROI size of $51 \times 51$ pixels, which suggests that such texture features could be used for purposes of segmenting regions of the cartilage matrix that are indicative of healthy or osteoarthritic chondrocyte organization. Such a segmentation algorithm would involve assigning a healthy or osteoarthritic label to every pixel in the radial zone based on texture features computed from the surrounding neighborhood. This would be useful in quantifying the percentage of the radial zone affected by OA, especially in cases where some portions of the cartilage remain healthy. Such quantitative measures could extend this study from a binary classification problem of differentiating between healthy and osteoarthritic cartilage samples to that of a bio-marker that tracks osteoarthritic progression in the cartilage matrix over time. This will be explored in further detail in future studies.

One limitation of this study was the small number of patients (five) from whom cartilage specimens were acquired for image acquisition. As a result, the classifier was trained with a smaller subset of patients and could be overtrained to the limited variations of healthy and osteoarthritic patterns found in these subjects. Future studies should include more patients to ensure that the classifier is trained with a potentially larger variation of healthy and osteoarthritic patterns. However, even with the small sample size used in this study, the separation between the two classes of chondrocyte patterns is adequately captured by high-dimensional feature vectors of Euler characteristic, as shown in Fig. 6. The inclusion of more patients would also enable extending our work for characterization of the entire patellar specimen based on local properties, and subsequent classification. We have taken a step in this direction by extracting texture features from smaller ROIs within each specimen, each of which be treated as a local neighborhood and the corresponding texture features characterize local spatial properties. Future studies could also focus on characterizing the alignment of chondrocytes in healthy ROIs where the current study focused more of the clustering of chondrocytes in osteoarthritic ROIs. Further improvements to textural characterization of chondrocyte organization could include volumetric analysis as both GLCM and MF can be computed for 3-D volumes of interest.

We also note a practical limitation with the experimental setup used in this study where the imaging technique relies on synchrotron radiation. This restricts its use to imaging *ex vivo* specimens such as those used in the study, rather than *in vivo* exams of the entire cartilage tissue, since the radiation source is stationary. Future research will be necessary to investigate the possibility of implementing PCI methods with high-brilliance and high-energy compact X-ray sources that are currently under development [44]-[46]. These technologies currently show significant promise for transferring PCI-CT imaging from synchrotron radiation facilities, which offer highly collimated, high fluence, and partially coherent X-rays, to a clinical environment. Another advantage of PCI-CT is its promising potential to save radiation by employing higher energy X-rays for the image acquisition which may be associated with a lower effective radiation dose for the patient [13]. The results of our *proof-of-principle* study demonstrate the potential role that PCI-CT could play in OA detection, which suggests that an implementation of an adapted PCI setup in one of these new sources could have a great impact in OA diagnosis.

## V. Conclusion

This study introduced an automated and nonsubjective computer-aided diagnosis approach in the context of PCI-CT for purposes of characterizing chondrocyte organization observed in the radial zone of the cartilage matrix of *ex vivo* human patella specimens. Our results suggest that textural characterization with topological features such as Euler characteristic or second-order statistical features such as correlation can provide high-classification performance in distinguishing between healthy and osteoarthritic ROIs annotated in this region. We hypothesize that such texture features could serve as PCI-based diagnostic bio-markers for evaluation and monitoring of OA.

## Acknowledgments

## REFERENCES

[1]. Woolf A, Pfleger B. Burden of major musculoskeletal conditions. Bull. World Health Org. 2003; 81:646–656. [PubMed: 14710506]

[2]. Yelin E. Cost of musculoskeletal diseases: Impact of work disability and functional decline. J. Rheumatol. 2003; 68:8–11.

[3]. Maclean C, Knight K, Paulus H, Brook R, Shekelle P. Costs attributable to osteoarthritis. J. Rheumatol. 1998; 25(11):2213–2218. [PubMed: 9818666]

[4]. Eckstein F, Wirth W, Nevitt M. Recent advances in osteoarthtiris imaging—The osteoarthritis initiative. Nature Rev.: Rheumatol. 2012; 8:622–630. [PubMed: 22782003]

[5]. Raya J, Horng A, Dietrich O, Krasnokutsky S, Beltran L, Storey P, Reiser M, Recht M, Sodickson D, Glaser C. Radiology. 2012; 262(2):550–559. [PubMed: 22106350]

[6]. Crema M, Roemer F, Marra M, Burstein D, Gold G, Eckstein F, Baum T, Mosher T, Carrino J, Guermazi A. Articular cartilage in the knee: Current MR imaging techniques and applications in clinical practice and research. Radiographics. 2011; 31(1):37–61. [PubMed: 21257932]

[7]. Hunter D, Le Graverand M-P, Eckstein F. Radiologic markers of osteoarthritis progression. Curr. Opin. Rheumatol. 2009; 21(2):110–117. [PubMed: 19339920]

[8]. Eckstein F, Glaser C. Measuring cartilage morphology with quantitative magnetic resonance imaging. Semin. Musculoskeletal Radiol. 2004; 8(4):329–353.

[9]. Bashir A, Gray M, Boutin R, Burstein D. Glycosaminoglycan in articular cartilage: In vivo assessment with delayed Gd(DTPA)(2-)-enhanced MR imaging. Radiology. 1997; 205(2):551–558. [PubMed: 9356644]

[10]. Reddy R, Li S, Noyszewski E, Kneeland J, Leigh J. Magn. Reson. Med. 1997; 38(2):207–214. [PubMed: 9256099]

[11]. Stahl R, Luke A, Li X, Carballido-Gamio J, Ma C, Majumdar S, Link T. Eur. Radiol. 2009; 19(1):132–143. [PubMed: 18709373]

[12]. Schmitt B, Zbyn S, Stelzeneder D, Jellus V, Paul D, Lauer L, Bachert P, Trattnig S. Radiology. 2011; 260(1):257–264. [PubMed: 21460030]

[13]. Coan P, Bamberg F, Diemoz P, Bravin A, Timpert K, Mützel E, Raya J, Adam-Neumair S, Reiser M, Glaser C. Characterization of osteoarthritic and normal human patella cartilage by computed tomography X-ray phase-contrast imaging: A feasibility study. Investigat. Radiol. 2010; 45(7):437–444.

[14]. Snigirev A, Snigireva I, Kohn V, Kuznetsov S, Schelokov I. On the possibility of X-ray phase contrast microimaging by coherent high-energy synchrotron radiation. Rev. Sci. Instrum. 1995; 66(12):5486–5492.

[15]. Davis T, Gao D, Gureyev T, Stevenson A, Wilkins S. Phasecontrast imaging of weakly absorbing materials using hard X-rays. Nature. 1995; 373:595–598.

[16]. Takeda T, Momose A, Itai Y, Jin W, Hirano K. Phase-contrast imaging with synchrotron X-rays for detecting cancer lesions. Acad. Radiol. 1995; 2(9):799–803. [PubMed: 9419642]

[17]. Keyriläinen J, Fernández M, Karjalainen-Lindsberg M, Virkkunen P, Leidenius M, von Smitten K, Sipilä P, Fiedler S, Suhonen H, Suortti P, Bravin A. Toward high-contrast breast CT at low radiation dose. Radiology. 2008; 249:321–327. [PubMed: 18796684]

[18]. Schneider T, Coan P, Habs D, Reiser M. Application of brilliant X-rays in mammography: Development and perspectives of phase contrast techniques. Der Radiologe. 2008; 48(4):345–350. [PubMed: 18311554]

[19]. Coan P, Mollenhauer J, Wagner A, Muehleman C, Bravin A. Analyzer-based imaging technique in tomography of cartilage and metal implants: A study at the ESRF. Eur. J. Radiol. 2008; 68(3):41–48.

[20]. Muehleman C, Majumdar S, Issever A, Arfelli F, Menk R, Rigon L, Heitner G, Reime B, Metge J, Wagner A, Kuettner K, Mollenhauer J. X-ray detection of structural orientation in human articular cartilage. Osteoarthritis Cartilage. 2004; 12(2):97–105. [PubMed: 14723869]

[21]. Chapman D, Thomlinson W, Johnston R, Washburn D, Pisano E, Gmür N, Zhong Z, Menk R, Arfelli F, Sayers D. Diffraction enhanced X-ray imaging. Phys. Med. Biol. 1997; 42(11):2015–2025. [PubMed: 9394394]

[22]. Bravin A. Exploiting the X-ray refraction contrast with an analyser: The state of the art. J. Phys. D: Appl. Phys. 2003; 36(10 A):24–29.

[23]. Connor D, Benveniste H, Dilmanian F, Kritzer M, Miller L, Zhong Z. Computed tomography of amyloid plaques in a mouse model of Alzheimer's disease using diffraction enhanced imaging. NeuroImage. 2009; 46(4):908–914. [PubMed: 19303447]

[24]. Haralick RM, Shanmuga K, Dinstein I. Textural features for image classification. IEEE Trans. Syst., Man, Cybern. Nov.1973 SMC-3(6):610–621.

[25]. Michielsen K, Raedt H. Integral-geometry morphological image analysis. Phys. Rep. 2001; 347(6):461–538.

[26]. Korfiatis P, Kalogeropoulou C, Karahaliou A, Kazantzi A, Skiadopoulos S, Costaridou L. Texture classification-based segmentation of lung affected by interstitial pneumonia in high-resolution CT. Med. Phys. 2008; 35(12):5290–5302. [PubMed: 19175088]

[27]. Nagarajan M, Huber M, Schlossbauer T, Leinsinger G, Krol A, Wismüller A. Classification of small lesions on breast MRI: Evaluating the role of dynamically extracted texture features through feature selection. J. Med. Biol. Eng. 2013; 33(1):59–68.

[28]. Wilhjelm JE, Gronholdt MLM, Wiebe B, Jespersen SK, Hansen LK, Sillesen H. Quantitative analysis of ultrasound B-mode images of carotid atherosclerotic plaque: Correlation with visual classification and histological examination. IEEE Trans. Med. Imag. Dec.1998 17(6):910–922.

[29]. Boehm H, Fink C, Attenberger U, Becker C, Behr J, Reiser M. Automated classification of normal and pathologic pulmonary tissue by topological texture features extracted from multi-detector CT in 3D. Eur. Radiol. 2008; 18(12):2745–2755. [PubMed: 18618121]

[30]. Huber M, Nagarajan M, Leinsinger G, Eibel R, Ray L, Wismüller A. Performance of topological texture features to classify fibrotic interstitial lung disease patterns. Med. Phys. 2011; 38(4):2035–2044. [PubMed: 21626936]

[31]. Nagarajan, M.; Huber, M.; Schlossbauer, T.; Leinsinger, G.; Krol, A.; Wismüller, A. Machine Vision and Applications. Springer-Verlag; New York, NY, USA: 2012. Classification of small lesions in dynamic breast MRI: Eliminating the need for precise lesion segmentation through spatiotemporal analysis of contrast enhancement.

[32]. Boehm H, Vogel T, Panteleon A, Burklein D, Bitterling H, Reiser M. Differentiation between post-menopausal women with and without hip fractures: Enhanced evaluation of clinical DXA by topological analysis of the mineral distribution in the scan images. Osteoporosis Int. 2007; 18(6):779–787.

[33]. Drucker H, Burges C, Kaufman L, Smola A, Vapnik V. Support vector regression machines. Adv. Neural Inf. Process. Syst. 1996; 9:155–161.

[34]. Pritzker K, Gay S, Jimenez S, Ostergaard K, Pelletier J-P, Revell P, Salter D, van den Berg W. Osteoarthritis cartilage histopathology: Grading and staging. Osteoarthritis Cartilage. 2006; 14:13–29. [PubMed: 16242352]

[35]. Ingal V, Beliaevskaya E. X-ray plane-wave topography observation of the phase contrast from a non-crystalline object. J. Phys. D: Appl. Phys. 1995; 28(11):2314–2317.

[36]. Fiedler S, Bravin A, Keyriläinen J, Fernández M, Suortti P, Thomlinson W, Tenhunen M, Virkkunen P, Karjalainen-Lindsberg M. Imaging lobular breast carcinoma: comparison of synchrotron radiation DEI-CT technique with clinical CT. Phys. Med. Biol. 2004; 49(2):175–188. [PubMed: 15083665]

[37]. Brankov J, Wernick M, Yang Y, Li J, Muehleman C, Zhong Z, Anastasio M. A computed tomography implementation of multipleimage radiography. Med. Phys. 2006; 33(2):278–289. [PubMed: 16532932]

[38]. Coan P, Peterzol A, Fiedler S, Ponchut C, Labiche J, Bravin A. Evaluation of imaging performance of a taper optics CCD 'FReLoN' camera designed for medical imaging. J. Synchrotron Radiat. 2006; 13(3):260–270. [PubMed: 16645252]

[39]. Dilmanian F, Zhong Z, Ren B, Wu X, Chapman L, Orion I, Thomlinson W. Computed tomography of X-ray index of refraction using the diffraction enhanced imaging method. Phys. Med. Biol. 2000; 45(4):933–946. [PubMed: 10795982]

[40]. Anys H, He D. Evaluation of textural and multipolarization radar features for crop classification. IEEE Trans. Geosci. Remote Sens. Sep.1995 33(5):1170–1181.

[41]. Chang, C-C.; Lin, C-J. LIBSVM: A library for support vector machines; ACM Trans. Intell. Syst. Technol. 2011. p. 27:1-27:27.[Online]. 2Software Available: http://www.csie.ntu.edu.tw/~cjlin/libsvm

[42]. Wright SP. Adjusted P-values for simultaneous inference. Biometrics. 1992; 48(4):1005–1013.

[43]. Holm S. A simple sequentially rejective multiple test procedure. Scand. J. Statist. 1979; 6(2):65–70.

[44]. Hirai T, Yamada H, Sasaki M, Hasegawa D, Morita M, Oda Y, Takaku J, Hanashima T, Nitta N, Takahashi M, Murata K. Refraction contrast 11x-magnified x-ray imaging of large objects by MIRRORCLE-type table-top synchrotron. J. Synchrotron Radiat. 2006; 13:397–402. [PubMed: 16924136]

[45]. Grüner F, Becker S, Schramm U, Eichner T, Fuchs M, Weingartner R, Habs D, Meyer-ter Vehn J, Geissler M, Ferrario M, Serafini L, van der Geer B, Backe H, Lauth W, Reiche S. Design considerations for table-top, laser-based VUV and X-ray free electron lasers. Appl. Phys. B. 2007; 86(3):431–435.

[46]. Habs D, Hegelich M, Schreiber J, Gross M, Henig A, Kiefer D, Jung D. Dense laser-driven electron sheets as relativistic mirrors for coherent production of brilliant X-ray and $\gamma$-ray beams. Appl. Phys. B. 2008; 93(2-3):349–354.
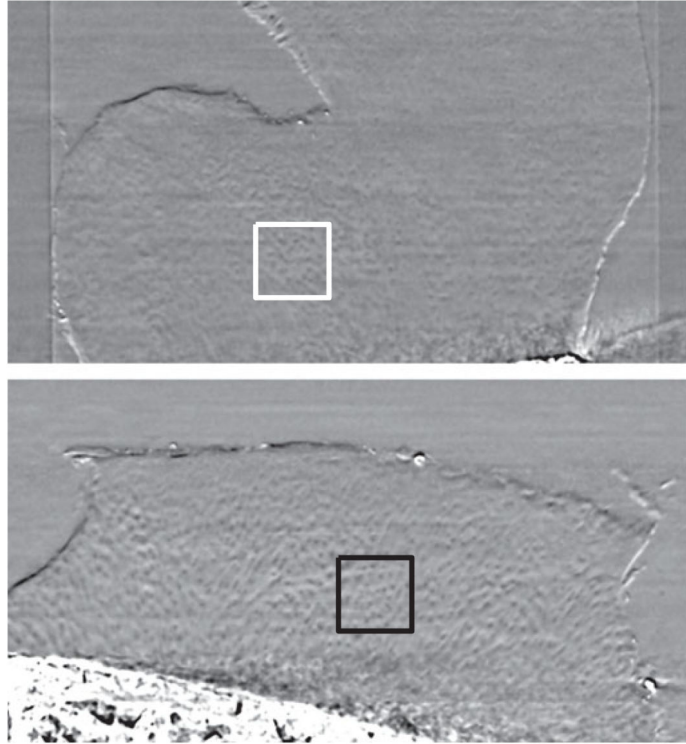
**Fig. 1.**
Coronal reconstructions of healthy (top) and osteoarthritic (bottom) cartilage specimens as visualized by PCI-CT. The boxes are representative of ROIs annotated in this study.
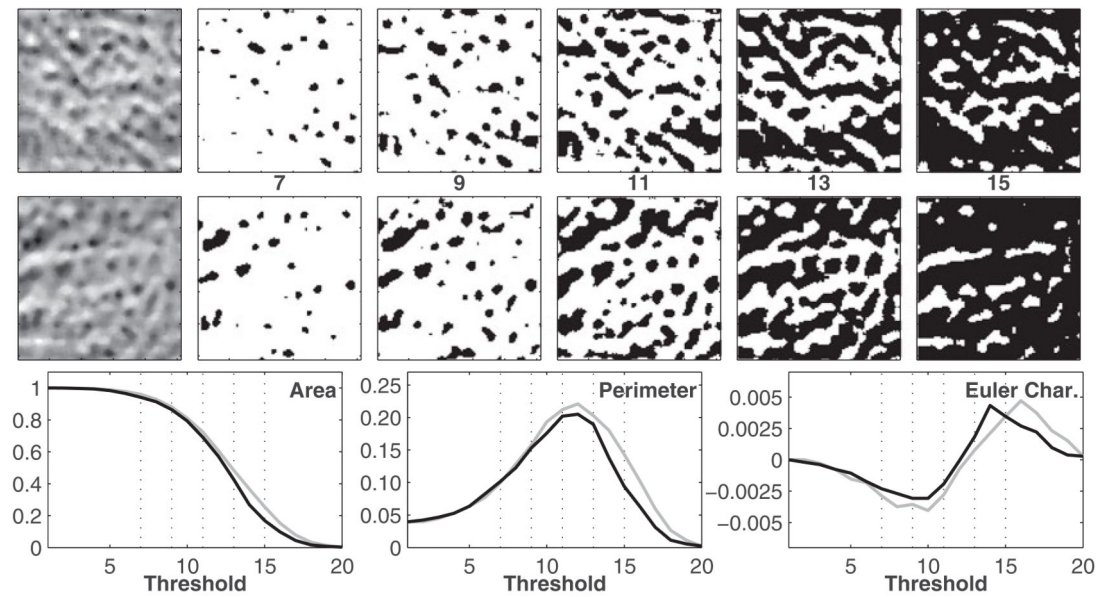
**Fig. 2.**
Illustration of MF. The upper and middle rows correspond to normal and osteoarthritic ROIs as shown in Fig. 1. The ROIs on the far left are binarized for five thresholds. In the bottom row, the three MF features—area, perimeter, and Euler characteristic, are plotted as a function of the threshold for the healthy (gray) and osteoarthritic (black) ROIs; the subset of the five thresholds (of 20) used to create the binary images are marked as vertical-dotted lines. These curves depict the morphological properties of the binary images and distinguish between healthy and osteoarthritic patterns.
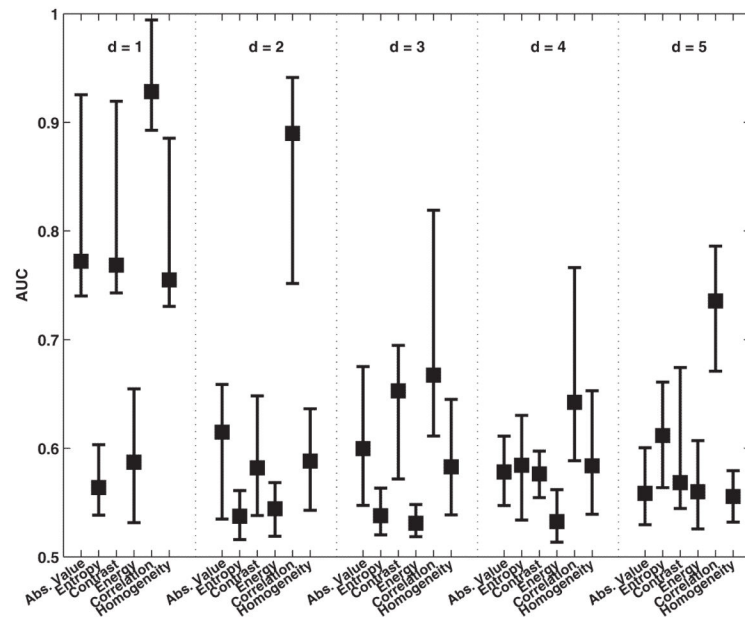
**Fig. 3.**
Comparison of classification performance achieved with GLCM when different interpixel distances (*d*) are used for computation of features. For each distribution, the central mark corresponds to the median and the edges are the 25th and 75th percentile. The best results are observed for correlation when *d* = 1.
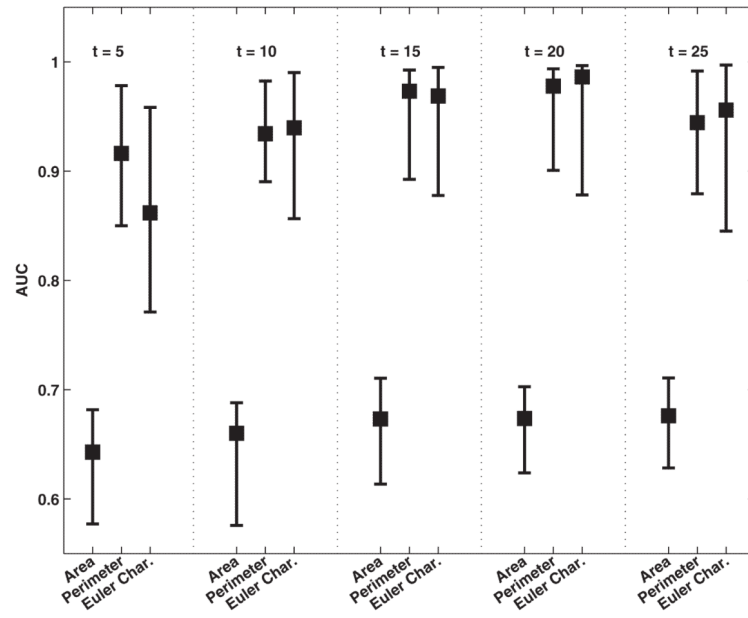
**Fig. 4.**
Comparison of classification performance achieved with the MF when different thresholds (*t*) are used for computation of features. For each distribution, the central mark corresponds to the median and the edges are the 25th and 75th percentile. The best results are obtained with Euler characteristic for 20 thresholds; increasing the number of thresholds further did not yield significantly better results.
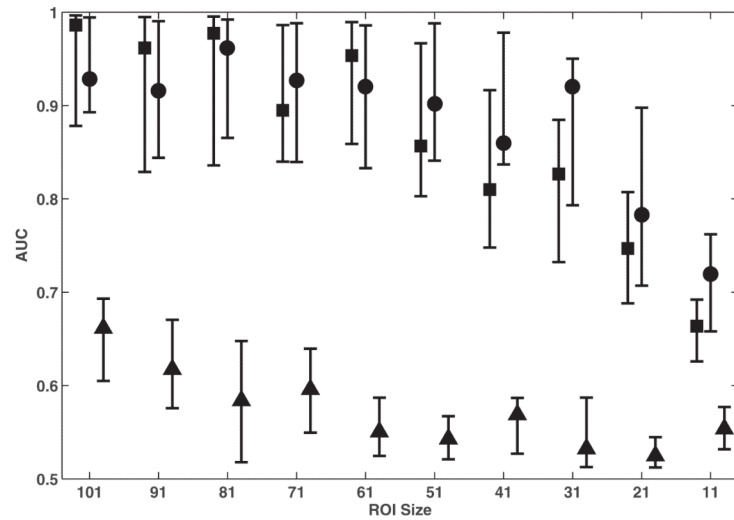
**Fig. 5.**

Comparison of classification performance achieved with Euler characteristic (square), correlation (circle), and standard deviation (triangle) when extracted from ROIs of different sizes. For each distribution, the central mark corresponds to the median and the edges are the 25th and 75th percentile. The best results are observed for the largest ROI size of $101 \times 101$ pixels; Euler characteristic and correlation exhibits the best performance when extracted from such ROIs.
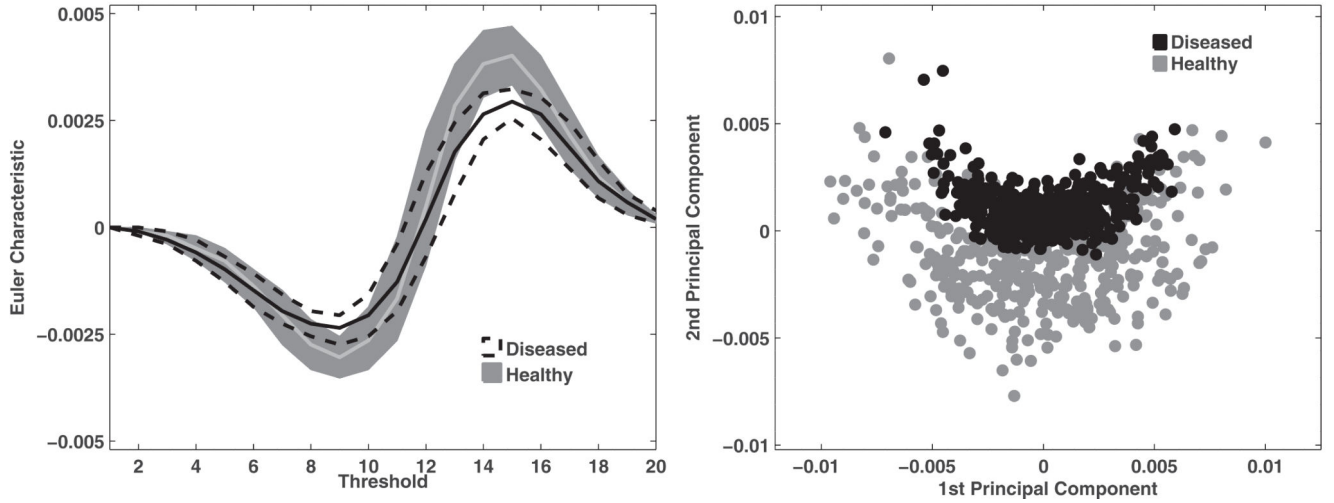
**Fig. 6.**
Illustration of the high-dimensional feature space of MF Euler characteristic. LEFT: The two corridors represent the Euler characteristic feature distribution for healthy (gray) and osteoarthritic (black) ROIs. Each corridor is enclosed by the standard 25th and 75th percentile as a function of the threshold; the solid lines represent the median. RIGHT: 2-D representation of the Euler characteristic feature space using the first two principal components computed from principal component analysis (PCA). As seen here, the Euler characteristic provides suitable discrimination between healthy and osteoarthritic ROIs.

**TABLE 1**

Comparison of Classification Performance (Mean AUC ± std) Achieved With Statistical Moments, GLCM Features and MF.

| Technique | Feature | AUC |
|---|---|---|
| Minkowski Functionals | Area | 0.67 ± 0.06 |
| | Perimeter | 0.94 ± 0.08 |
| | Euler Characteristic | **0.94 ± 0.07** |
| GLCM | Absolute Value | 0.78 ± 0.12 |
| | Entropy | 0.57 ± 0.04 |
| | Contrast | 0.78 ± 0.13 |
| | Energy | 0.59 ± 0.06 |
| | Correlation | **0.93 ± 0.07** |
| | Homogeneity | 0.76 ± 0.12 |
| Statistical Moments | Mean | 0.55 ± 0.04 |
| | Std | 0.66 ± 0.06 |
| | Mean & Std | 0.62 ± 0.07 |

The best results (bold) are obtained with Euler characteristic (MF), Perimeter (MF), and correlation (GLCM).